# Octupole correlations near $^{110}$Te

D. A. Testov ⬤,[1,2,3] S. Bakes,[1,2,4] J. J. Valiente-Dobón,[5] A. Goasduff,[1,2] S. Frauendorf,[6] F. Nowacki,[7] T. R. Rodríguez,[8]
G. de Angelis,[5] D. Bazzacco,[2] C. Boiano,[9] A. Boso,[1,2] B. Cederwall,[10] M. Cicerchia,[1,5] P. Čolović,[11] G. Colucci,[1,2,12]
F. Didierjean,[7] M. Doncel,[13] J. A. Dueñas ⬤,[14] F. Galtarossa,[5] A. Gozzelino,[5] K. Hadyńska-Klęk,[5,12] G. Jaworski,[5,12]
P. R. John,[15] S. Lenzi,[1,2] H. Liu,[10] S. Lunardi,[1,2] R. Menegazzo,[2] D. Mengoni,[1,2] A. Mentana,[9] D. R. Napoli,[5] G. Pasqualato,[1,2]
F. Recchia,[1,2] S. Riccetto,[16] L. M. Robledo,[8] M. Rocchini,[17,18,*] B. Saygi,[19,†] M. Siciliano,[5,‡] Yu. Sobolev,[3] and S. Szilner[11]

[1]*Dipartimento di Fisica Astronomia dell' Università di Padova, Padova 35131, Italy*
[2]*INFN, Sezione di Padova, Padova 35131, Italy*
[3]*Joint Institute for Nuclear Research, Dubna, Moscow region 141980, Russia*
[4]*Department of Physics, University of Surrey, Surrey GU2 7XH, United Kingdom*
[5]*INFN, Laboratori Nazionali di Legnaro, Legnaro 35020, Italy*
[6]*Department of Physics, University Notre Dame, Indiana 46556, USA*
[7]*Institut Pluridisciplinaire Hubert CURIEN (IPHC), Strasbourg 67200, France*
[8]*Departamento de Física Tetórica and Centro de Investigacitón Avanzada en Física Fundamental,*
*Universidad Autónoma de Madrid, Madrid 28049, Spain*
[9]*Dipartimento di Fisica dell' Università di Milano and INFN, Sezione di Milano, Milano 20133, Italy*
[10]*KTH Royal Institute of Technology, Stockholm SE-100 44, Sweden*
[11]*Ruder Bošković Institute, Zagreb 10000, Croatia*
[12]*Heavy Ion Laboratory, University of Warsaw, Warsaw 02-093, Poland*
[13]*The University of Liverpool, Liverpool L69 3BX, United Kingdom*
[14]*Departamento de Ingeniería Eléctrica y Centro de Estudios Avanzados en Física,*
*Matemáticas y Computación, Universidad de Huelva, Huelva 21007, Spain*
[15]*Institut für Kernphysik, Technische Universität Darmstadt, Darmstadt 64289, Germany*
[16]*Dipartimento di Fisica e Geologia dell'Università di Perugia and INFN, Sezione di Perugia, Perugia 06123, Italy*
[17]*Università degli Studi di Firenze, Florence 50121, Italy*
[18]*INFN, Sezione di Firenze, Florence 50019, Italy*
[19]*Department of Physics, Faculty of Science, Ege University, Izmir 35040, Turkey*

The lifetime of the $2^+$ and $9^-$, $11^-$, $13^-$, $15^-$ states in the neutron-deficient $^{110}$Te was measured for the first time using the recoil distance Doppler shift technique. The reported value of the reduced transition probability $B(E2; 0^+_{g.s} \rightarrow 2^+) = 4.3(8) \times 10^3 \, e^2 fm^4$ supports the systematic for even-mass Te isotopes and was interpreted in the framework of the large-scale shell model and cranked shell model calculations. The measured reduced transition probabilities in the negative-parity yrast band revealed the upward trend towards the high spins. The enhanced collectivity is discussed in terms of the tilted axis cranking approach and the symmetry configuration mixing method with the Gogny D1S interaction.

## I. INTRODUCTION

The existence of nuclei with stable deformed shapes was realized early in the history of nuclear physics. The observation of large quadrupole moments led to the suggestion that some nuclei might have spheroidal shapes, which was confirmed by the observation of rotational band structures.

Since such shapes are symmetric under the space inversion, all members of the rotational band have the same parity. Instead, nuclei that represent reflection-asymmetric shapes, as for example the pear shape, develop low-lying negative-parity states. Based on extensive investigations of this kind of deformations it was concluded that they are not as stable as the familiar quadrupole deformations. The octupole correlations that generate reflection-asymmetric shapes are generated microscopically by the interaction between orbitals of opposite parity differed by three units of angular momentum near the Fermi surface. In general this situation occurs when the Fermi level lies between the intruder-orbital and the normal parity subshell. These correlations happen in well-defined areas of the Segrè chart, when the number of protons or neutrons is equal to 32, 56, 90—octupole magic numbers [1–3].

---

*Present address: University of Guelph, Department of Physics, N1G2W1 Guelph, Canada.

†Present address: Faculty of Science and Arts, Department of Physics, Sakarya University, Sakarya 54187, Turkey.

‡Present address: Physics Department, Argonne National Laboratory, Lemont IL 60439, USA.
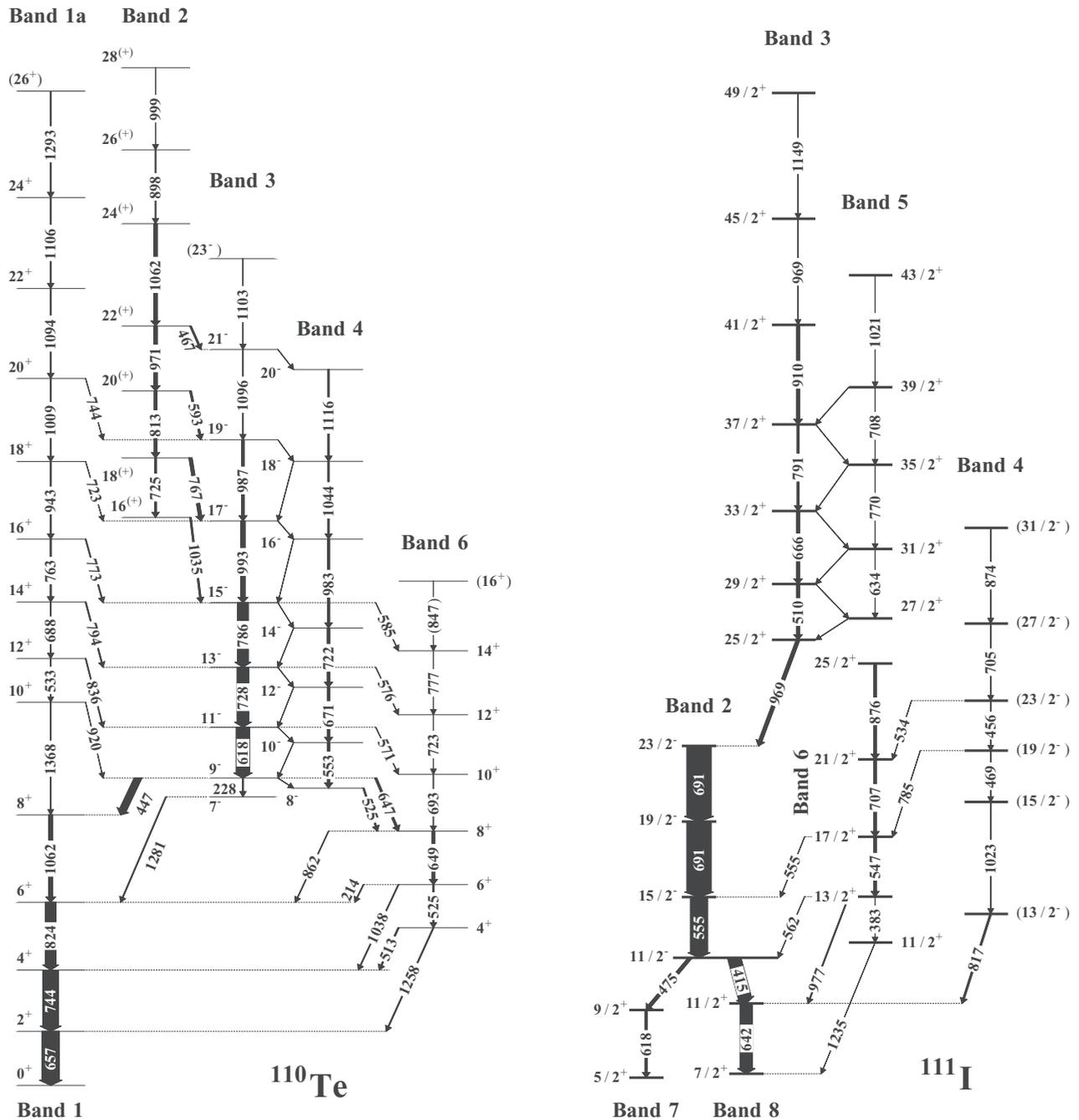
FIG. 1. Partial level schemes of $^{110}$Te and $^{111}$I relevant to the discussion. Level energy, spin-parity assignment, and intensities are from [13,18]; the arrow width is proportional to the transition intensity.

One of the regions in which it is predicted the ground-state octupole deformation is the region near $^{122}$Ba [4]. Indeed, the enhancement of $E1$ transitions was experimentally observed in tellurium [5–7] and xenon nuclei [8–12]. The spectacularly high $B(E1) \approx 10^{-3}$ W.u. strengths, reported for $^{110}$Te, are the largest for all tellurium isotopes [13] and are comparable to those known in Ra-Th region, where the strongest octupole effects are found.

A closer look on $^{110}$Te reveals that the structure of its low-spin levels is different from its neighbors. In heavier isotopes (i.e., $^{112}$Te [14], $^{114}$Te [15]) the yrast levels continue

as positive parity states up to high spins and are interpreted in terms of the aligned $\nu[h_{11/2}]^2$ structure [16]. However, in $^{110}$Te because of the Fermi surface, which lies below the $\nu h_{11/2}$, the $\nu[h_{11/2}]^2$ configuration is not favored allowing, thus the negative-parity configurations to compete, and the negative-parity sequence becomes yrast, see Fig. 1. Indeed, the drop of intensities in the positive parity band above the $8^+$ state was observed [13]. The low-lying negative states were interpreted as two-quasineutron configuration $\nu[h_{11/2} \otimes d_{5/2}]$. These orbitals differ in both $l$ and $j$ by 3, and one can expect octupole softness already at low spin for $^{110}$Te. The weakness

to octupole deformation of light tellurium isotopes towards the octupole magic number $N = 56$ is predicted in the Strutinsky calculations in Ref. [17]. The enhanced $E1$ transitions in $^{110}$Te between positive and negative parity bands $2 \rightarrow 3$; bands 1a $\rightarrow 3$ (band numbering as in Fig. 1) were observed [13]. Noticeably, band 2 decays to band 3 by $E1$ transitions, which are extremely fast in comparison with the in-band ones. Similar enhancement of $E1$ transition appears in $^{109}$Te between bands $2 \rightarrow 1$ and bands $3 \rightarrow 4$ (band numbering as in Ref. [6]); and in $^{111}$I between bands $6 \rightarrow 2$ and $4 \rightarrow 6$ (band numbering as in Fig. 1). This systematic appearance of strong $E1$ transitions can be attributed to the specific band configurations containing the octupole admixtures. Therefore, in the present paper we discuss the nature of octupole correlations in $^{110}$Te based on the deduced $B(E2; I \rightarrow I - 2)$ transition strengths. For the first time it is reported the lifetime of $2^+$, $11^-$, $13^-$, and $15^-$ states. The experimental details are given in Sec. II. The shell-model description to $B(E2; 0^+_{g.s} \rightarrow 2^+)$ is discussed in Sec. III A. The performed tilted axis cranking (TAC) and symmetry conserving configuration mixing calculations (SCCM) summarized in Sec. III B and Sec. III C, respectively, suggest that the pattern of the $E1$ transitions is more consistent with an admixture of octupole vibrations to the reflection symmetric configurations.

## II. EXPERIMENTAL DETAILS

The experiment was performed at the National Legnaro Laboratories using a 2 pnA beam of $^{58}$Ni delivered by XTU-Tandem. Excited states in $^{110}$Te were populated in the $^{58}$Ni($^{58}$Ni, $1\alpha2p$) reaction. A $^{58}$Ni beam impinged at 250 MeV into a 1 mg/cm$^2$ $^{58}$Ni target followed by a 15 mg/cm$^2$ Au-stopper foil. The detector setup, shown in Fig. 2, was similar to one described in Ref. [19]. Emitted $\gamma$ rays were detected by the GALILEO $\gamma$-ray spectrometer. In Phase I [20] it consisted of 25 Compton-suppressed HPGe tapered detectors, originally from the GASP array [21]. Detectors were arranged into four rings. Three backward rings were made of five detectors each at $\Theta_0 = 152°$, $\Theta_1 = 129°$, and $\Theta_2 = 119°$ measured with respect to the beam direction. The last ring at $\Theta_3 = 90°$ comprised ten detectors. Lifetimes were determined via the recoil distance doppler-shift (RDDS) method [22] using a deferential plunger device [23]. The channel selection was provided by the EUCLIDES Si-array [24]. To allow installation of the plunger device in the reaction chamber the backward positioned $\Delta E$-$E$ Si-telescopes of EUCLIDES were removed. In this configuration EUCLIDES had five segmented $\Delta E$-$E$ telescopes placed at the forward angles of $\approx 30°$ and ten single-plate telescopes arranged in the second forward ring at $\approx 60°$ with respect to the beam direction. The technical details on the EUCLIDES Si-array in the plunger configurations are reported in a separate publication [19].

In the off-line analysis the $1\alpha2p$ channel leading to $^{110}$Te was selected by requiring a condition that only events in coincidence with $1\alpha$ and $1p$ or $1\alpha$ and $2p$ were incremented in $E_\gamma$-$E_\gamma$ matrices. To derive the lifetime of the level of interest the intensities of shifted $(I^B_s I^A_s)$ and unshifted $(I^B_s I^A_u)$ components of a depopulating transition $A$ gating on the shifted component of a populating transition $B$ in particle
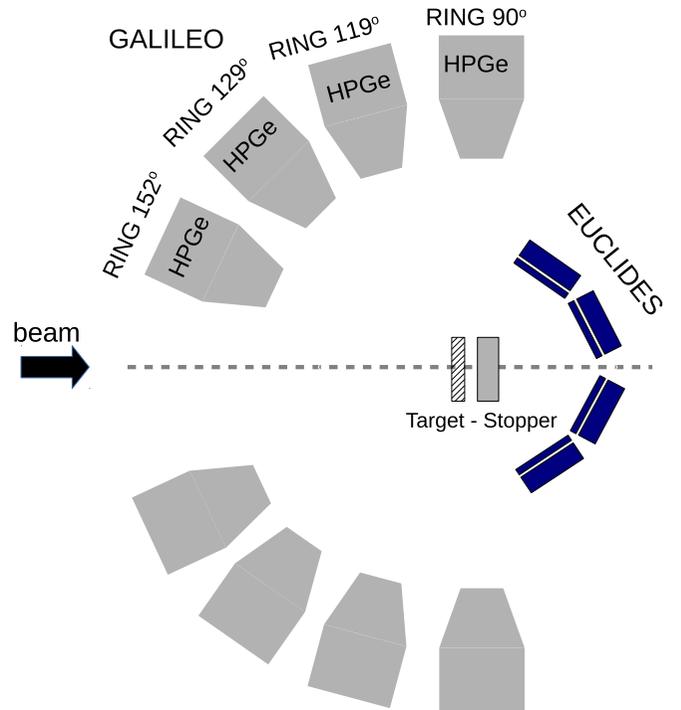


FIG. 2. Schematic view of the GALILEO $\gamma$-ray spectrometer coupled to 15 forward-most $\Delta E$-$E$ telescopes of EUCLIDES. The target and stopper, installed at the center of the reaction chamber, are schematically illustrated. See text for more details.

gated $E_\gamma$-$E_\gamma$ matrices were measured. The lifetime of a state ($\tau$) was derived using the differential decay curve method (DDCM) [22]:

$$\tau = \frac{I^B_s I^A_u(x)}{\frac{d}{dx} I^B_s I^A_s(x)} \frac{1}{v},\tag{1}$$

where $\frac{d}{dx} I^B_s I^A_s(x)$ denotes the derivative of the shifted component of the transition $A$. The lifetime fits were done using the NAPATAU software [25]. The recoil velocity $v$ was deduced by the Doppler-shifted energy of various transitions belonging to $^{110}$Te in each detector ring at angles greater than $\Theta_3 = 90°$. The mean value of $v = 3.5(1)\%$ of the speed of light was inferred for the recoil of interest. The measured lifetime of a state is mutually related to the transition probability by equations listed in the textbook, see Ref. [26]. Using these equations, the branching ratios reported in Ref. [13] and the internal conversion coefficients from Ref. [27] the $B(E2 \uparrow)$ values were derived.

### A. $2^+$ state

To determine the lifetime of the $2^+$ state in $^{110}$Te data were acquired for six target-to-stopper distances ranged between 112 $\mu$m and 696 $\mu$m. For each distance the intesity of both shifted and unshifted (stopped) components of $\gamma$ rays was obtained by calculating the areas under both peaks, in the spectra derived from the recorded $E_\gamma$-$E_\gamma$ particle gated matricies, by imposing a gate on the shifted component of the $4^+$ transition of 744 keV. Spectra presented in Fig. 3
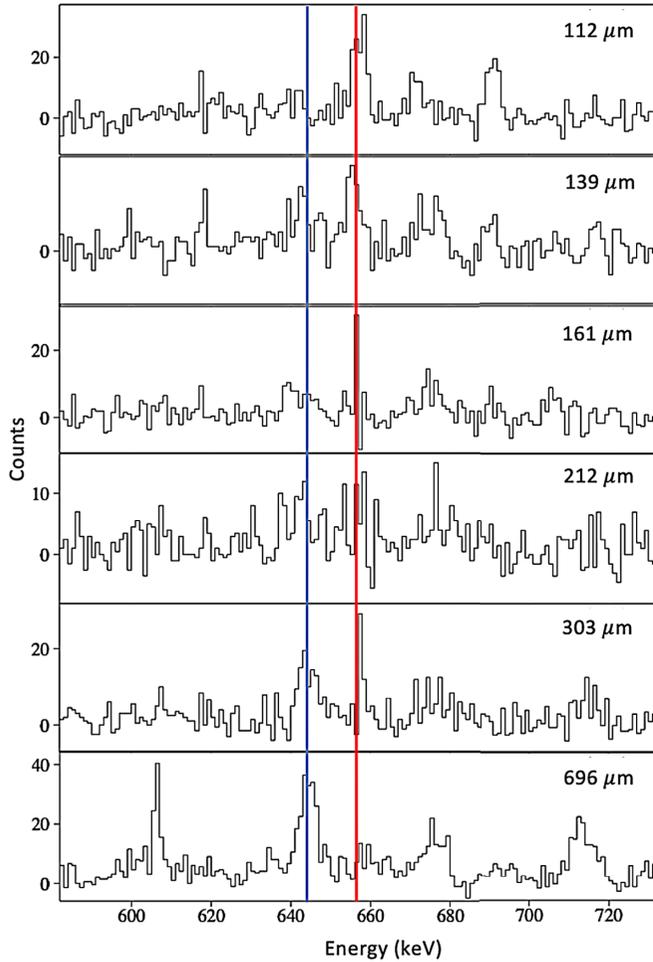
FIG. 3. Coincidence $E_\gamma$-$E_\gamma$ spectra conditioned by charged particles and gated on the shifted component of the $4^+ \rightarrow 2^+$ feeding transition in ring $\Theta_0$. The shifted (at 645 keV) and stopped (at 657 keV) components of the depopulating transition recorded by $\Theta_2$ ring are indicated by left (blue) and right (red) lines correspondingly.

illustrate the quality of the data. The $\tau$ curve of the $2^+$ state and the intensities of stopped and shifted components of the $2^+ \rightarrow 0^+_{g.s.}$ as a function of distance $d$ are shown in Fig. 4. It can be also seen that the $\tau$ value is practically constant with the distance, indicating that there is no side feeding into the $2^+$ state. The lifetime value adopted as the weighted average for six ring-to-ring combinations is $\tau_{2^+} = 7.7(1.4)$ ps. The deduced transition probability is $B(E2; 0^+_{g.s.} \rightarrow 2^+) = 4.3(8) \times 10^3 \ e^2 fm^4$, which translates into 137(28) W.u.

### B. Negative parity states

In $^{110}$Te the strong yrast transitions can be followed up to the spin $J^\pi = 8^+$. In heavier tellurium isotopes the yrast line continues as positive-parity states up to a higher spin and is interpreted in terms of the aligned $\nu[h_{11/2}]^2$ configuration. However, the Fermi surface in $^{110}$Te lies below $h_{11/2}$ making thus the $\nu[h_{11/2}]^2$ configuration energetically unfavored; and negative parity sequences can compete. Indeed, above the yrast positive-parity states (above $J^\pi = 8^+$) a strongly
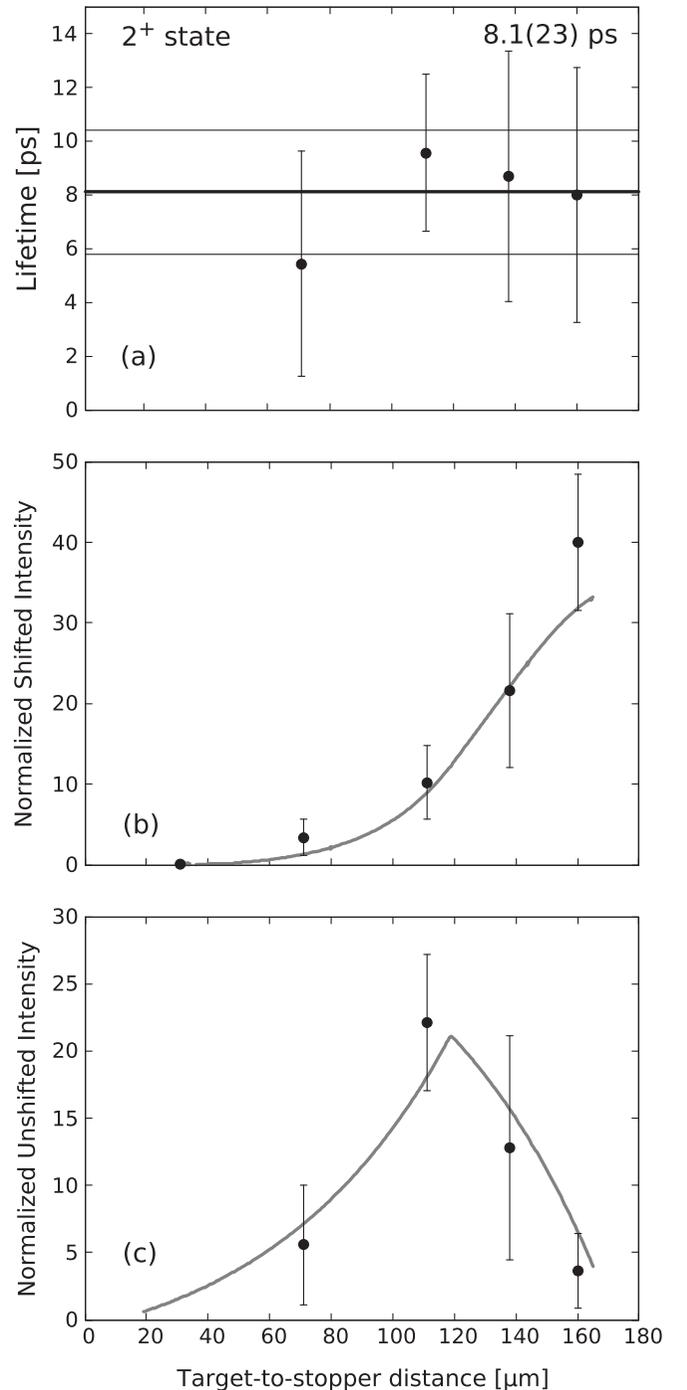


FIG. 4. $\tau$ curve of the $2^+$ state in $^{110}$Te measured using $\Theta_2$ ring with a gate on the feeding $4^+ \rightarrow 2^+$ transition in $\Theta_0$ ring; intensities of the (b) shifted and (c) stopped components of the $2^+ \rightarrow 0^+$ depopulating transition are plotted as a function of distance $d$. The lifetime obtained using the indicated ring combination for the sensitive region is shown in (a).

populated negative parity band 3 is observed. The structure is built on the $9^-$ bandhead and is based on the two-quasineutron $\nu[h_{11/2} \otimes d_{5/2}]$ configuration. The change of parity along the yrast line happens via the $9^- \rightarrow 8^+$ transition of 447 keV, which is the unique feature of all tellurium isotopes.
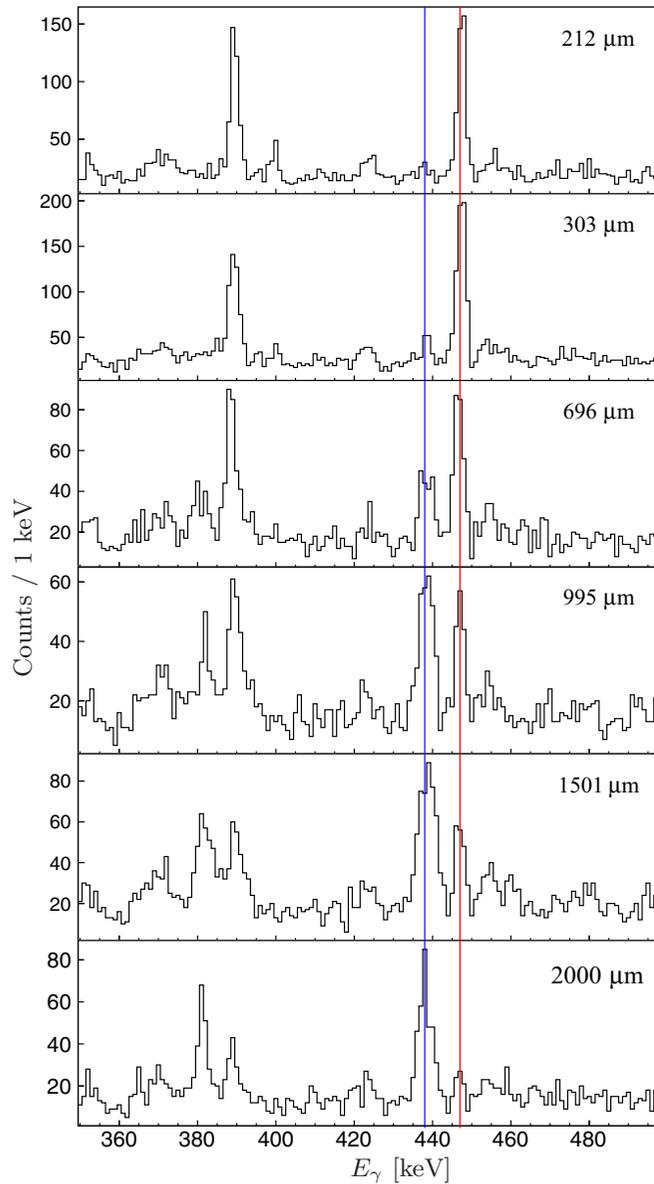
FIG. 5. Coincidence $E_\gamma$-$E_\gamma$ spectra conditioned by charged particles and gated on the shifted component of the $11^- \to 9^-$ feeding transition in ring $\Theta_0$. The shifted (at 439 keV) and stopped (at 447 keV) components of the depopulating transition recorded by $\Theta_2$ ring are indicated by left (blue) and right (red) lines correspondingly.

Moreover, below $J^\pi = 12^+$ band 1a carries so little intensity that a $\gamma$-ray transition of 1368 keV linking $10^+ \to 8^+$ states was only tentatively assigned in Ref. [13]. However, above $J^\pi = 12^+$ band 1a is linked by $E1$ transitions strongly populating the negative-parity band 3, which is another peculiarity of $^{110}$Te.

The lifetime of $9^-$ state was measured using six plunger-to-stopper distances ranged between $212\,\mu$m and $2000\,\mu$m. For each distance the intensity of shifted and unshifted (stopped) components of $\gamma$-rays was found by calculating the areas under both peaks in the spectra obtained from the $E_\gamma$-$E_\gamma$ particle gated matrices, imposing a gate on the shifted component of the $11^- \to 9^-$ transition. The spectra presented in



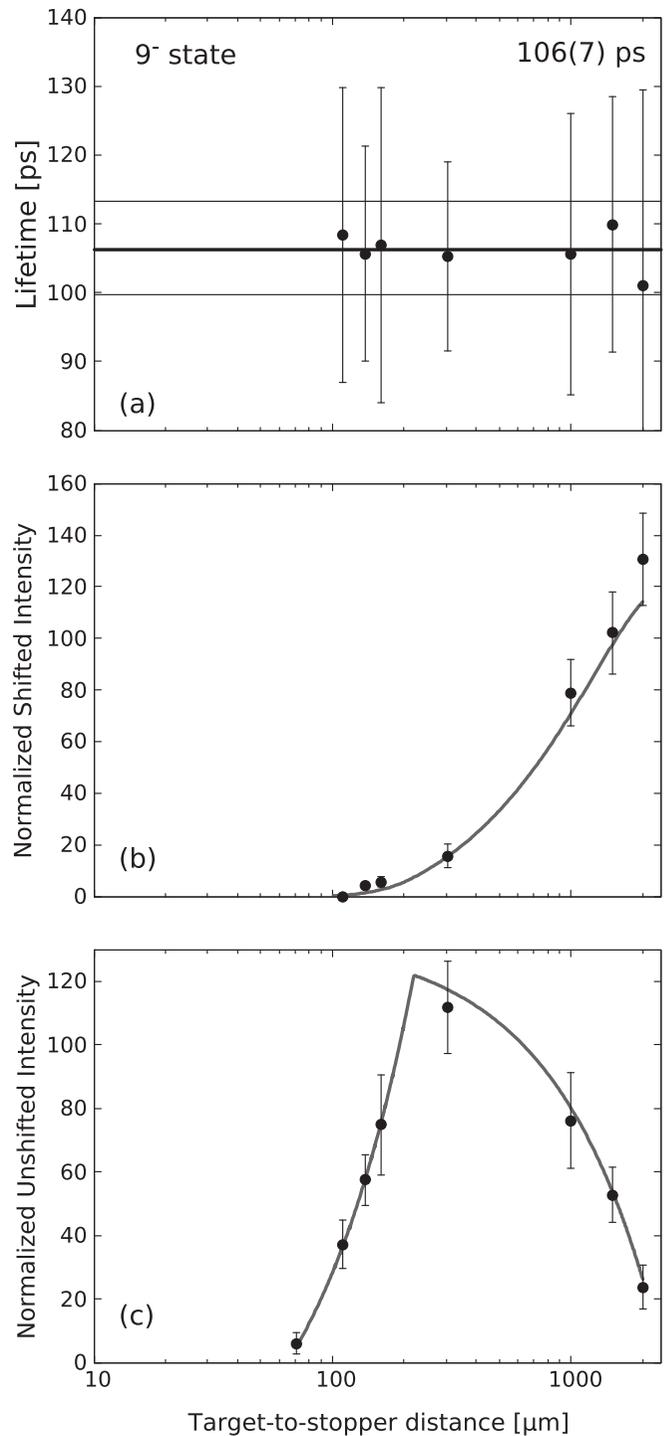FIG. 6. (a) $\tau$ curve of the $9^-$ in $^{110}$Te measured using $\Theta_2$ ring with a gate on the $11^- \to 9^-$ feeding transition in $\Theta_0$ ring; intensities of the (b) shifted and (c) stopped components of the $9^- \to 8^+$ depopulating transition are plotted as a function of distance $d$. The lifetime obtained using the indicated ring combination for the sensitive region is shown in (a).

Fig. 5 illustrate the quality of the data. The $\tau$-curve of the $9^-$ state and the intensities of stopped and shifted components of the $9^- \to 8^+$ transition as a function of distance $d$ are shown in Fig. 6. It can be also seen that the $\tau$ value is

TABLE I. Transition energies ($E_\gamma$) and measured lifetimes ($\tau_{exp}$) for the indicated states in $^{110}$Te.

| $^{110}$Te | $E_\gamma$ keV | $\tau_{exp}$ ps |
|---|---|---|
| $2^+$ | 657 | 7.7(14) |
| $9^-$ | 447 | 105.9(41) |
| $11^-$ | 618 | 6.6(5) |
| $13^-$ | 728 | 2.2(3) |
| $15^-$ | 786 | 1.4(4) |

practically constant with the distance indicating that there is no side feeding into the $9^-$ state. The lifetime value adopted as the weighted average for six ring-to-ring combinations is $\tau_{9^-} = 105.9(41)$ ps. The lifetime of $9^-$ state deduced in the present experiment is very long in comparison with what one can expect from the systematics. Most probable it indicates a configuration change, and the $9^-$ state is the head of a rotational band.

To determine the lifetimes of the $11^-$, $13^-$, $15^-$ state in $^{110}$Te, reported in Table I, the plunger-to-stopper distances, ranged between 21 $\mu$m to 301 $\mu$m, in which the slope of the fitted curve was well defined, were selected for the analysis. For each distance the intensity of shifted and unshifted (stopped) components of $\gamma$ rays were found by calculating the areas under both peaks in spectra obtained from the $E_\gamma$-$E_\gamma$ particle gated matrices, imposing a gate on a feeding transition to prevent contribution from possible side feeders. The adopted transition probabilities for these higher spin states in the band built on the $9^-$ bandhead are listed in Table II. Finally, the 1368 keV $\gamma$ ray tentatively assigned in Ref. [13] to link the $10^+ \to 8^+$ states was not observed in the coincidence $\gamma$-$\gamma$ analysis summing the data for all the distances.

## III. DISCUSSION

### A. Shell-model description

The systematics of $B(E2; 0^+_{g.s} \to 2^+)$ values for even-even Te isotopes represents a near-text book case showing the maximum collectivity at the middle of the shell and the single particle behavior towards the end of the shell. The $B(E2; 0^+_{g.s} \to 2^+)$ experimental trend was well described in the frame of the large-scale shell model (LSSM) [28], see Fig. 7. The $B(E2; 0^+_{g.s} \to 2^+)$ value for $^{110}$Te measured in the

TABLE II. Experimental $B(E2 \uparrow)$ values for the indicated transitions in $^{110}$Te in comparison with TAC and SCCM calculations.

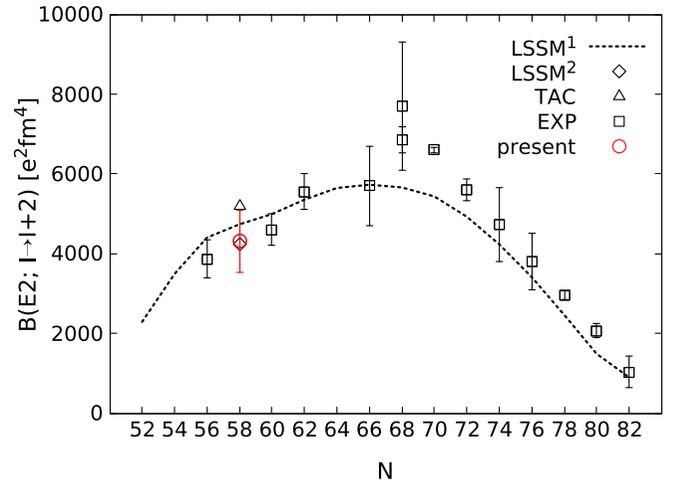| $^{110}$Te | $B(E2 \uparrow)$ ($e^2 fm^4$) | | |
|---|---|---|---|
| | exp | TAC | SCCM |
| $0^+ \to 2^+$ | 4312(785) | 5200 | 7490 |
| $7^- \to 9^-$ | 903(106) | – | 3494 |
| $9^- \to 11^-$ | 1608(199) | 1460 | 3887 |
| $11^- \to 13^-$ | 2034(397) | 1270 | 4442 |
| $13^- \to 15^-$ | 2143(682) | 1140 | 9721 |



FIG. 7. Measured $B(E2; 0^+_{g.s.} \to 2^+)$ sterngth in $^{110}$Te and the experimental $B(E2; 0^+_{g.s.} \to 2^+)$ data for the Te isotopic chain from the evaluator [29] in comparison with LSSM calculations from Ref. [28] (LSSM$^1$) and with the results of calculations from the present work: LSSM (LSSM$^2$) and TAC.

present work follows the systematics and is consistent with the shell model description. The reported value is also supported by our LSSM calculations performed in the frame of the Caurier-Nowacki approach [30] within the CD-Bonn [31] interaction in the $0g_{7/2}$, $1d_{5/2}$, $1d_{3/2}$, $1s_{1/2}$, and $0h_{11/2}$ model space using $e_n = 0.65e$ and $e_p = 1.35e$ effective charges.

### B. Cranking calculations

Our interpretation assumes that the octupole correlations have vibrational character. A harmonic vibrational excitation does not change the transition matrix element between the quadrupole-collective states based on a quasiparticle configuration. For this reason the cranking calculations for reflection symmetric shapes were carried out in the framework of the tilted axis cranking code (TAC) [32]. For the states relevant to the lifetime measurements the total Routhian was minimized with respect to the deformation parameters $\varepsilon$ and $\gamma$. The authors of Refs. [33,34] study the even-even Mo, Pd, and Cd isotopes with the similar neutron numbers along this line. Their TAC calculations account well for the experimental energies and $B(E2)$ values of the ground-state band, which have collective vibrational character, and are proportional to the spin of the initial states, as well as for $s$-band states after the back bend, which behave as a more rotational structure with approximately constant $B(E2)$ values. The studies demonstrate that TAC calculations provide a flexible microscopic description of transitional nuclei between these limits.

The experimental data on $E2$ transition probabilities for Te isotope are revealed in Fig. 8. The $^{118,120}$Te nuclei are in the middle of the shell and can be associated with the collective vibrational motion. The regularly spaced level spectra and the transition strengths are proportional to the spin of the initial states (i.e., $R_{4/2} = B(E2; 4^+ \to 2^+)/B(E2; 2^+ \to 0^+ \approx 2)$) make them a good example of quadrupole vibrators. However, $^{114}$Te is different: the almost equally spaced levels of the
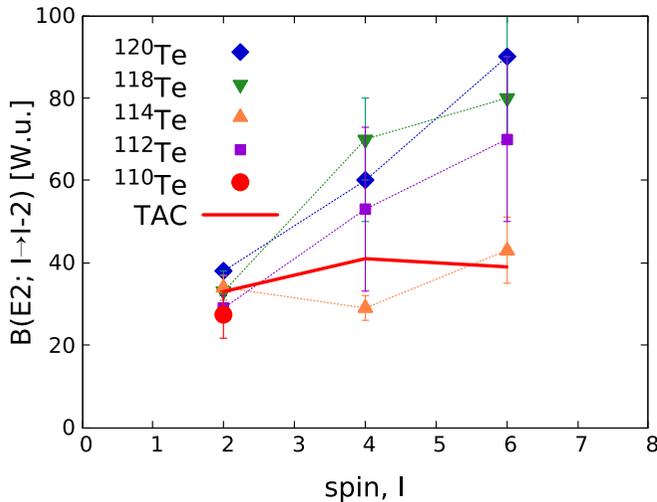
FIG. 8. TAC calculations for the intra-g.s.-band transitions as a function of the spin for $^{110}$Te (solid line) compared to the available experimental data for $^{110}$Te (present), $^{112}$Te [35], $^{114}$Te [36], $^{118}$Te [37], and $^{120}$Te [38].



FIG. 9. Adopted in the present work $B(E2\uparrow)$ values for the indicated transitions in $^{110}$Te plotted as a function of the spin in comparison with TAC and SCCM calculations.

ground state band suggest the vibrational behavior. It is in contrast to the almost constant $B(E2; I \rightarrow I-2)$ values and corresponds to a low ratio of $R_{4/2} \approx 1$, which is similar to that of a rotor. This observation was reproduced by a large-scale shell model study in Ref. [35]. The experimental data on the neighboring $^{112}$Te seem to point to a good vibrational system. But there is a contradiction to the large-scale shell model calculations, which give near-constant $B(E2; I \rightarrow I-2)$ trend for $^{112}$Te [35]. However, very large errors leave the question open, whether the data are in conflict with the calculations. Our results of TAC calculations for the intra-g.s.-band transitions in $^{110}$Te, plotted in Fig. 8, predict almost constant $B(E2; I \rightarrow I-2)$ values corresponding to a small $R_{4/2}$ ratio. The result for $^{112}$Te is similar and consistent with the large-scale shell model results of Ref. [35]. The data and calculations may point to a trend: in the middle of the neutron shell Te isotopes behave like collective vibrators. Towards the bottom of the shell the $B(E2; I \rightarrow I-2)$ values become less $I$ dependent, which can be understood as a transition to the seniority coupling scheme with $B(E2; I \rightarrow I-2)$ values that decreases with $I$.

The calculated $E2$ transition strengths, quoted in Table II and denoted by TAC in Figs 7 and 9, well account for the values deduced in the present experiment. In particular, the substantially smaller $B(E2; I-2 \rightarrow I)$ values of band 3, as compared to the $B(E2; 0^+ \rightarrow 2^+)$ strength, are reproduced. This reduction is a consequence of the deformation drive of the unpaired $h_{11/2}$ neutron, which is well established for the aligned $h_{11/2}$ neutron pair in the neutron $s$ bands [33]. However, the slight upward $B(E2; I-2 \rightarrow I)$ trend in band 3 is not reproduced. TAC estimations give rather a slight downward trend, which is typical for configurations containing high-$j$ intruder orbitals [33]. It is a response to the alignment of the high-$j$ orbitals with the rotational axis, which is common for terminating bands of weakly deformed nuclei and is experimentally confirmed for many cases. The octupole correlations generate a mixture of high-intruder orbitals with low-$j$
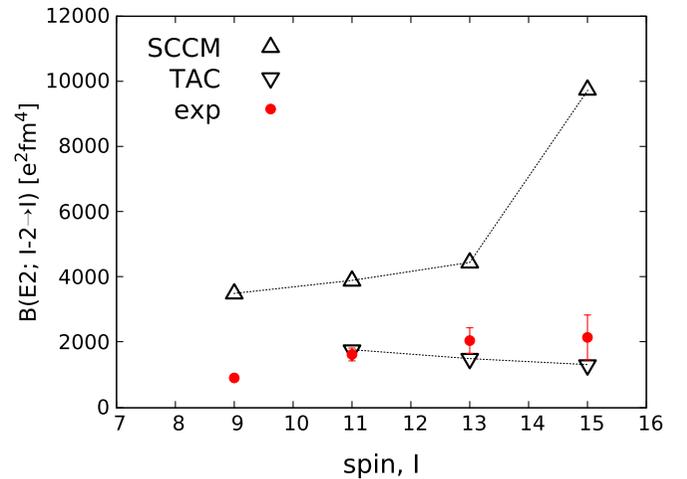
orbitals of the opposite parity, which drives the deformation in a different way. One may speculate that such a mixture may reverse the weak downward trend of the reflection-symmetric TAC calculation to the weak upward trend seen in the experiment. The $9^- \rightarrow 7^-$ transition could not be calculated, because the TAC code provides only transition probabilities within a band with the same quasiparticle configuration.

In contrast to even-even nuclei, where individual collective octupole vibrational excitations are observed, in odd-$A$ nuclei the collective octupole vibrational strength is fragmented over several states with dominant quasiparticle structures. The same is expected for high-spin states containing aligned quasiparticles. For this reason, it is appropriate to classify the bands according to their quasiparticle structure in a rotation reflection-symmetric potential.

The enhanced $E1$ transitions linking positive and negative band structures have been also reported for the $^{109}$Te [6] and $^{111}$I [18] odd-$A$ neighbors of $^{110}$Te. Therefore, we analyzed the band structures of these nuclei altogether in the framework of the cranked shell model. The cranking calculations were similar to ones performed in Refs. [6,13]. The calculations used the modified Nilsson potential with the deformation parameters $\epsilon_2 = 0.15$, $\epsilon_4 = 0.015$, $\gamma = 15°$ and pairing gaps $\Delta_p = 1.1$ MeV, $\Delta_n = 0$. The deformation parameters are close to the values determined self-consistently. As most of the configurations contain more than one excited quasineutron, the neutron pair gap was set to zero, at variance with Refs. [6,13]. The quasiproton and single-neutron levels for $^{110}$Te are shown in Fig. 10 (to be compared with Fig. 9 of Ref. [13]).

In the spirit of the cranked shell model, we assigned configurations to the bands in $^{110}$Te, $^{109}$Te, and $^{111}$I, see Table III. The configurations are based on the quasi-/single-particle Routhians, see Fig. 10, which assume zero octupole deformation and represent a consistent set. Following common practice, uppercase letters are assigned to the quasiproton and lowercase letters to the single-neutron routhians. The suggested configurations are listed in Table III. The notation is explained in the caption.

TABLE III. Configuration table for the known bands in $^{109}$Te, $^{110}$Te, $^{111}$I [6,13,18]. For $^{109}$Te the bands are labeled as in Ref. [6]. For $^{110}$Te and $^{111}$I the bands are labeled as Fig. 1. Parity and signature are denoted by $(\pi, \alpha)$. The configurations are identified by the letters attached to the single- and quasi-particle routhians shown in Fig. 10, which are the same as in Ref. [13]. The configurations are noted as follows. In case of the protons, 0 is the quasiparticle vacuum, and the letters indicate the routhians that are occupied by one quasiproton. In case of the neutrons, 0 denotes the configuration with all routhians at $\omega = 0$ occupied up to $N = 58$ and continued diabaticlly to higher $\omega$. The letters indicate particle-hole configuration relative to this configuration. The collective octupole vibration with odd spin (simplex +) is denoted by O. It is a mixture of the configurations EB, AF, eb$^{-1}$, fa$^{-1}$, and more small negative parity two-quasiproton and neutron particle-hole excitations. The columns proton and neutron indicate the respective configurations. The configurations agree with the ones assigned in Refs. [6,13,18].

| band | basic configuration | | $(\pi, \alpha)$ | octupole admixture | | enhanced $E1$ transitions |
| | proton | neutron | | proton | neutron | |
| --- | --- | --- | --- | --- | --- | --- |
| | | | $^{109}$Te | | | |
| 1 | 0 | ea$^{-1}$b$^{-1}$ | $(-, -1/2)$ | | | |
| 3 | 0 | fa$^{-1}$b$^{-1}$ | $(-, +1/2)$ | 0 | a$^{-1}$O | a$^{-1}$O $\rightarrow$ a$^{-1}$ |
| | | | | | | fa$^{-1}$b$^{-1}$ $\rightarrow$ fa$^{-1}$b$^{-1}$O (band 3 $\rightarrow$ 4) |
| 4 | 0 | b$^{-1}$ | $(+, -1/2)$ | 0 | fa$^{-1}$b$^{-1}$O | |
| 6 | 0 | ca$^{-1}$b$^{-1}$ | $(+, +1/2)$ | | | |
| 2 | BE | ea$^{-1}$b$^{-1}$ | $(+, +1/2)$ | 0 | ea$^{-1}$b$^{-1}$O | ea$^{-1}$b$^{-1}$O $\rightarrow$ ea$^{-1}$b$^{-1}$ (band 2 $\rightarrow$ 1) |
| 5 | 0 | da$^{-1}$b$^{-1}$ | $(+, -1/2)$ | | | |
| | | | $^{111}$I | | | |
| 7 | A | 0 | $(+, 1/2)$ | | | |
| 8 | B | 0 | $(+, -1/2)$ | | | |
| 1 | E | efa$^{-1}$b$^{-1}$ | $(-, -1/2)$ | | | |
| 2 | E | 0 | $(-, -1/2)$ | CO | 0 | |
| 6 | C | 0 | $(+, 1/2)$ | EO | 0 | EO $\rightarrow$ E |
| | | | | | | C $\rightarrow$ CO (band 6 $\rightarrow$ 2) |
| 3 | E | eb$^{-1}$ | $(+, 1/2)$ | EO | 0 | EO $\rightarrow$ E (band 3 $\rightarrow$ 2) |
| 5 | E | ea$^{-1}$ | $(+, -1/2)$ | | | |
| 4 | C | a$^{-1}$e | $(-, -1/2)$ | CO | 0 | CO $\rightarrow$ C (band 4 $\rightarrow$ 6) |
| | | | $^{110}$Te | | | |
| 1 | 0 | 0 | $(+, 0)$ | | | |
| 1a | 0 | efa$^{-1}$b$^{-1}$ | $(+, 0)$ | 0 | ea$^{-1}$O | ea$^{-1}$O $\rightarrow$ ea$^{-1}$ |
| | | | | | | efa$^{-1}$b$^{-1}$ $\rightarrow$ efa$^{-1}$b$^{-1}$O (band 1a $\rightarrow$ 3) |
| 3 | 0 | ea$^{-1}$ | $(-, 1)$ | 0 | efa$^{-1}$b$^{-1}$O | |
| | | | | 0 | db$^{-1}$O | |
| 4 | 0 | eb$^{-1}$ | $(-, 0)$ | | | |
| 2 | EF | 0 | $(+, 0)$ | 0 | ea$^{-1}$O | ea$^{-1}$O $\rightarrow$ ea$^{-1}$ (band 2 $\rightarrow$ 3) |
| 6 | 0 | db$^{-1}$ | $(+, 0)$ | 0 | ea$^{-1}$O | db$^{-1}$O $\rightarrow$ db$^{-1}$ |
| | | | | | | ea$^{-1}$ $\rightarrow$ ea$^{-1}$O (band 3 $\rightarrow$ 6) |

Similarly to $^{110}$Te the enhancement of the $B(E1)$ strength was observed in $^{109}$Te for transitions between bands 2 $\rightarrow$ 1 and 3 $\rightarrow$ 4; and in $^{111}$I between bands 6 $\rightarrow$ 2 and 4 $\rightarrow$ 6, see Fig. 11. As indicated in the configuration Table III, $E1$ transitions connect bands of the same simplex quantum number, which suggests that the enhancement is caused by an admixture of simplex-conserving octupole modes (they have a reflection plane perpendicular to the symmetry axis, see Ref. [39] for details).

To support the configuration band assignment in $^{110}$Te, Fig. 12(b) shows the alignment $I_x$ as a function of the rotational frequency $\hbar\omega$. Clearly the TAC results correlate well with the data. The alignment values calculated for the relevant two-neutron configurations are [efa$^{-1}$b$^{-1}$]: 9.54, [ea$^{-1}$]: 5.37, [eb$^{-1}$]: 4.56. The order is consistent with the TAC calculations, however, the calculated differences are

larger than the experimental ones. The cranking calculations do not allow us to generate angular momentum below $I_x \approx 9$ for the [eb] configuration, which suggests that the 9$^-$ should be interpreted as the bandhead, and the 7$^-$ state belongs to another configuration.

Table III and Fig. 11 demonstrate that the systematic appearance of enhanced $E1$ transitions in $^{109}$Te, $^{110}$Te, and $^{111}$I can be attributed to the admixture of a simplex $+ (\pi = -, I$ odd) octupole vibration (denoted by O) to the assigned band configurations. The admixture of the octupole vibration may explain why differences of the alignment $I_x$ between the configurations [efa$^{-1}$b$^{-1}$], [ea$^{-1}$], and [eb$^{-1}$] are smaller in the experiment than obtained by the reflection-symmetric cranking calculations, see Fig. 12(b). The octupole correlations mix the high-$j$ intruder orbitals with the low-$j$ normal parity orbitals, which reduces the alignment
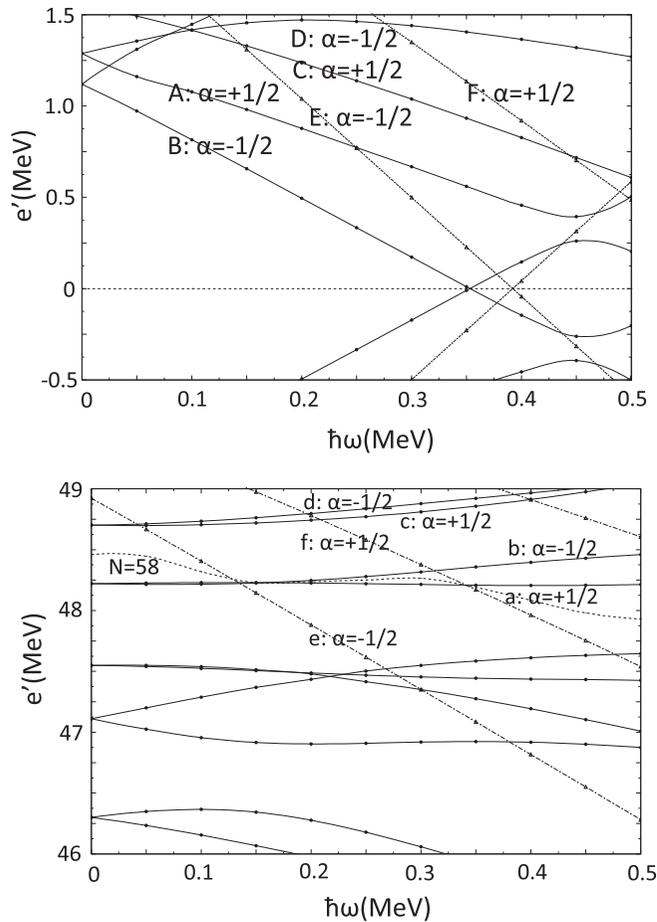
FIG. 10. (a) Proton quasiparticle and (b) neutron single particle routhians for $Z = 52$, $N = 58$, with $\pi = +$ (solid line), and $\pi = -$ (dashed line).



FIG. 11. Energies of the bands minus the energy of $0.4\,I$ MeV. For $^{109}$Te the bands are labeled as in Ref. [6]. For $^{110}$Te and $^{111}$I the bands are labeled as Fig. 1. Full symbols show states with $I = 2n$ or $I = 1/2 + 2n$ and open symbols states with $I = 1 + 2n$ or $I = -1/2 + 2n$ ($n$ integer). The arrows indicate enhanced $E1$ transition.

difference between the two kinds of orbitals. The reduction can be seen by comparing the quasiparticle routhians of the axial-symmetric and the octupole-deformed potential (see, e.g., Refs. [1,3]).

Figure 12(a) shows that the yrast line has a trend that is nearly linear (a straight tangent). As seen more clearly in Fig. 11(c) the yrast (or yrare) line is composed of band sequences, which alternate in parity and signature (fixed simplex) connected by $E1$ transitions. That is the signature of the octupole phonon condensation scenario [40]. Because of the mixed 2qp-octupole phonon nature, it appears not as clean as in the cases from the actinides region [41,42]. The relative alignments of the various bands are not three as for the purely collective octupole phonons. There is a deviation of the yrast line from being linear at high spins, which indicates the end of the condensation regime (or being only part of the mechanism that generates the angular momentum).

The conclusion is that there is no clear classification into collective octupole excitations carrying three units of alignment and two-quasiparticle excitations of negative parity. The mixed character of the states is seen from the relative alignments of the groups, which differ both from the value of three for a collective octupole excitation and from the values
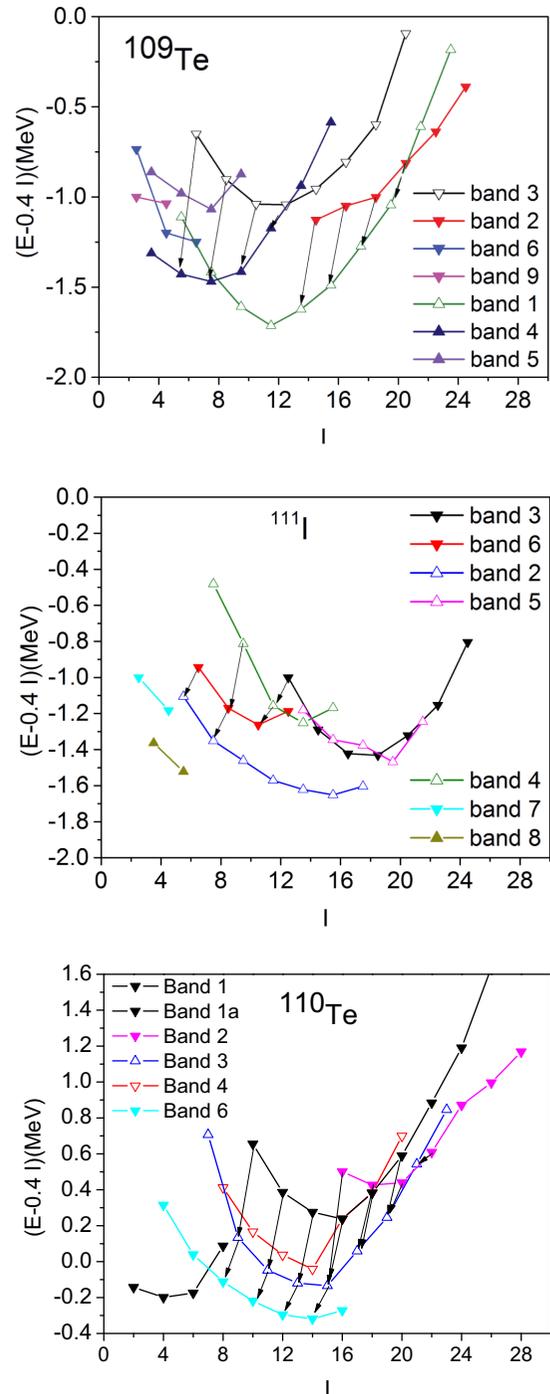
obtained by adding the alignments of the excited two quasiparticles. The configuration assignment combined with the octupole admixtures is impressively consistent. One should also take into account that the octupole phonon contains the $\pi = -$ components of the two quasiparticles that are excited. Therefore, the octupole admixtures are different for different
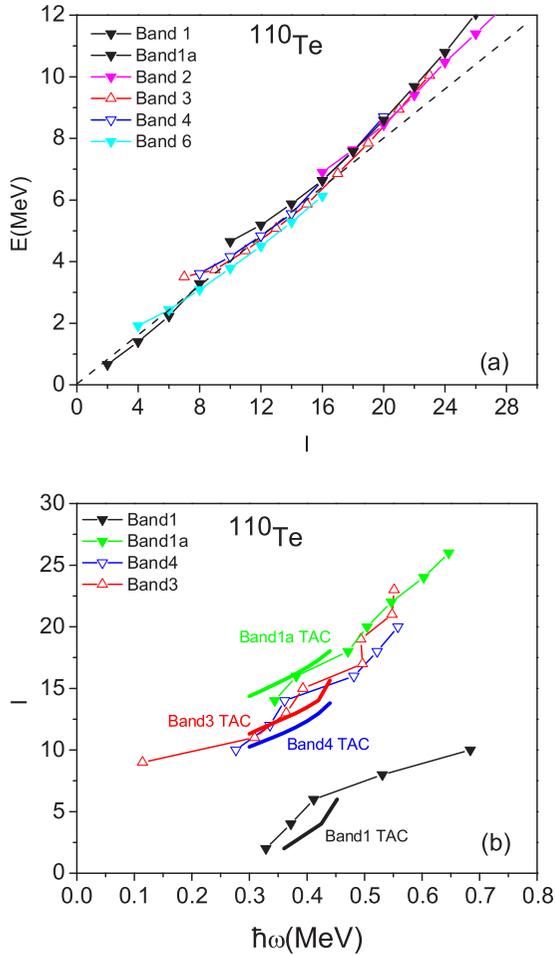
FIG. 12. (a) Experimentally known energies of the bands in $^{110}$Te as a function of the spin. The bands are labeled as in Fig. 1, full symbols denote even $I$ and open symbols odd $I$ states. The dashed line shows the energy subtracted in Fig. 11. (b) Angular momentum $I$ as a function of the rotational frequency $\hbar\omega(I) = (E(I) - E(I-2))/2$. Comparison of TAC calculations (solid lines denoted by "TAC") with the known experimental data.

pairs. According to the Pauli Principle, the explicitly indicated quasiparticles are blocked in the collective configuration of the octupole phonon O.

### C. Beyond mean-field calculations

The data were also interpreted in the framework of the symmetry conserving configuration mixing (SCCM) calculations with the Gogny D1S interaction [43]. The present implementation of the method included the mixing of intrinsic states with different axial quadrupole and octupole deformations ($\beta_2$, $\beta_3$) to describe negative parity bands [44]. The intrinsic states were found by performing constrained Hartree-Fock-Bogoliubov (HFB) calculations and, subsequently, simultaneous parity, particle-number, and angular momentum projection. The final nuclear states, from which excitation energies and transition probabilities were computed, were obtained within the generator coordinate method
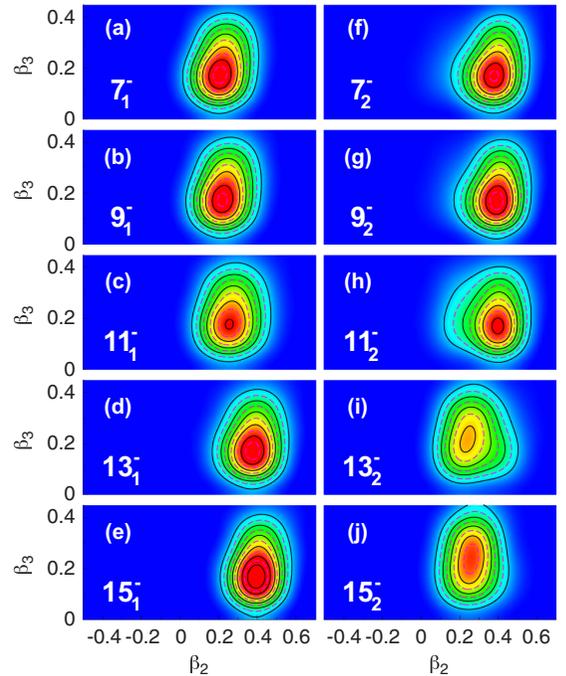


FIG. 13. Collective wave functions in the ($\beta_2$, $\beta_3$) plane for the two lowest negative parity states calculated using the axial SCCM method including parity symmetry breaking.

(GCM). In the present work, neither triaxial shapes nor time-reversal symmetry breaking states were included because of the huge computational burden and the current limitations of the existing codes. As a consequence, this approach did not allow for the description of spin alignments. The spectrum is expected to be stretched because the ground-state energy is favored over the energies of excited states. Despite these limitations, this SCCM method allowed the qualitative description of positive and negative parity low-lying states in Ba isotopes [44–46].

In our case, we are interested in the description of the negative parity high-spin states. In Fig. 9 the experimental and theoretical $B(E2)$ values are shown. The calculated transition strengths overestimate the experimental values, but they follow the experimental upward trend. The results can be understood in terms of the collective wave functions, which represent the probability for the deformation parameters $\beta_2$ an $\beta_3$ in each individual nuclear state.

In Fig. 13 we show the collective wave functions of the lowest two negative parity rotational bands obtained in the SCCM calculations. We observe two distinctive structures with similar octupole deformations $\beta_3 \approx 0.20$ but different prolate quadrupole deformations, $\beta_2 \approx 0.25$ and $\beta_2 \approx 0.40$, respectively. The former configuration is the yrast negative parity band up to $J^\pi = 11^-$ where a sudden crossing to the more deformed branch is found. Hence, the $B(E2)$ values slightly increase from the $7^- \to 9^-$ to the $9^- \to 11^-$ transitions because they are members of the same rotational bands; the $B(E2; 11^- \to 13^-)$ value also increases a bit because the partial mismatch between the collective wave function is compensated by the larger deformation of the $J^\pi = 13^-$ state; finally, the $B(E2; 13^- \to 15^-)$ is the largest because the states

belong to the same rotational band and the quadrupole deformation is larger. The global overestimation of the theoretical values with respect to the experiment is partially due to the use of Gogny energy density functional combined with exact angular momentum restoration, which tends to predict larger deformations in the whole isotopic chain [47]. As discussed above, a more reliable description of the negative parity band can be achieved by including time-reverse symmetry breaking states and combining the full triaxial quadrupole and octupole degrees of freedom on the equal footing. However, this kind of calculations is far from being possible considering the present energy density codes and computational limits.

In contrast to the SCCM, the TAC calculations take the alignment of $h_{11/2}$ neutrons into account, which in terms of SCCM corresponds to the neglected time-odd components. As discussed above, it is the unpaired aligned $h_{11/2}$ neutron that reduces the deformation. When quasiparticle alignment sets in, the deformation goes down, which has been seen in many calculations (see, e.g., Ref. [33]). This important polarization is missing in the SCCM. As a consequence, the SCCM calculations give a too large deformation comparable with the value for the $0^+$ and $2^+$ states. Accordingly, the $B(E2)$ values of band 3 are close to the $B(E2; 0^+ \to 2^+)$ value.

## IV. CONCLUSIONS

The GALILEO $\gamma$-ray spectrometer coupled to the EU-CLIDES Si-array and to the plunger device was used to measure the lifetimes of excited states in $^{110}$Te. The nucleus was populated using the $^{58}$Ni($^{58}$Ni, $\alpha$2p) reaction. The lifetime of the $2^+$ state in the g.s. band, the $9^-$ bandhead state as well as the $11^-$, $13^-$, and $15^-$ states was measured for the first time. The reported $B(E2; 2^+ \to 0^+)$ transition probability is in line with the systematic for even-even Te isotopes. The performed large-scale shell model calculations using CD-Bonn potential confirm the experimental value. The cranked mean-field calculations based on the shell correction method further support our measurement. The calculations, in contrast to the vibrational-like picture, predict almost a constant behavior of the $B(E2; I \to I–2)$ dependence as a function of the spin. The similar trend, observed in the neighboring $^{114}$Te nucleus, represents a challenge for understanding.

The observed $B(E2; I - 2 \to I)$ values in the negative parity sequence are about a factor of two smaller than the $B(E2; 2^+ \to 0^+)$ strength. The reduction of the $B(E2)$ values can be caused by the unpaired rotational-aligned $h_{11/2}$ neutron, which drives the deformation toward smaller values. The same cranked mean-field calculations reproduce well the experimental results. The slightly upward experimental trend was explained by the beyond-mean-field approach based on the Gogny D1S effective interaction. The performed angular momentum and parity projected generator coordinate calculations, including axial quadrupole and octupole degrees of freedom are able to give a qualitative agreement but overestimate the experimental $B(E2)$ values. The discrepancy could be attributed to the overestimation of the quadrupole deformation with the SCCM method that uses an interaction fitted to mean-field properties. In addition, the present SCCM calculations neglect the time-odd components of the mean field, which would allow for the rotational alignment of the unpaired $h_{11/2}$ neutron, that also reduces the deformation of the system. Such calculations including time-reversal symmetry breaking is still far from being possible with the present energy density functional codes and computing capabilities.

The cranked shell model approach allowed us to analyze the $^{110}$Te band structure and its odd-$A$ neighbors $^{109}$Te and $^{111}$I. A consistent set of quasiparticle configuration in the reflection-symmetric rotating potential was assigned. The observed pattern of enhanced $E1$ transitions between bands of opposite parity could be explained by an admixture of an octupole vibration of simplex +.

[1] P. A. Butler and W. Nazarewicz, Rev. Mod. Phys. **68**, 349 (1996).

[2] R. H. Spear and W. N. Catford, Phys. Rev. C **41**, 1351(R) (1990).

[3] S. Frauendorf and V. V. Pashkevich, Phys. Lett. B **141**, 23 (1984).

[4] P. Möller *et al.*, At. Data Nucl. Data Tables **59**, 185 (1995).

[5] G. J. Lane *et al.*, Phys. Rev. C **57**, R1022 (1998).

[6] A. J. Boston *et al.*, Phys. Rev. C **61**, 064305 (2000).

[7] E. S. Paul *et al.*, Phys. Rev. C **50**, 698 (1994).

[8] H. C. Scraggs *et al.*, Phys. Rev. C **61**, 064316 (2000).

[9] G. de Angelis *et al.*, Phys. Lett. B **535**, 93 (2002).

[10] E. S. Paul, H. R. Andrews, T. E. Drake, J. DeGraaf, V. P. Janzen, S. Pilotte, D. C. Radford, and D. Ward, Phys. Rev. C **53**, 2520 (1996).

[11] E. S. Paul *et al.*, Nucl. Phys. A **644**, 3 (1998).

[12] J. Timár *et al.*, J. Phys. G **21**, 783 (1995).

[13] E. S. Paul *et al.*, Phys. Rev. C **76**, 034322 (2007).

[14] E. S. Paul *et al.*, Phys. Rev. C **75**, 014308 (2007).

[15] C. B. Moon *et al.*, Phys. Rev. C **51**, 2222 (1995).

[16] E. S. Paul, H. R. Andrews, T. E. Drake, J. DeGraaf, V. P. Janzen, S. Pilotte, D. C. Radford, and D. Ward, Phys. Rev. C **50**, R534 (1994).

[17] J. Skalski, Phys. Lett. B **238**, 6 (1990).

[18] P. Spolaore *et al.*, Nucl. Phys. A **682**, 387 (2001).

[19] J. Bradbury *et al.*, Nucl. Inst. Meth. A **979**, 164345 (2020).

[20] A. Goasduff *et al.* (unpublished).

[21] D. Bazzacco, in *Workshop on Large γ-ray Detector Arrays* No. AECL10613 (Chalk River Laboratories, Canada, 1992), p. 376.

[22] A. Dewald *et al.*, Prog. Part. Nucl. Phys. **67**, 786 (2012).

[23] C. Müller-Gatermann *et al.*, Nucl. Inst. Meth. A **920**, 95 (2019).
[24] D. Testov *et al.*, Eur. Phys. J. A **55**, 47 (2019).
[25] B. Saha, Program NAPATAU, Ph.D. thesis, Institute for Nuclear Physics, Universität zu Köln, Cologne, 2004.
[26] H. Morinaga and T. Yamazaki, *In-Beam Gamma-Ray Spectroscopy* (North-Holland, Amsterdam, Netherlands, 1976), p. 68.
[27] https://www.nndc.bnl.gov/ensdf/.
[28] Chong Qi, Phys. Rev. C **94**, 034310 (2016).
[29] https://www.nndc.bnl.gov/be2/.
[30] A. Banu *et al.*, Phys. Rev. C **72**, 061305(R) (2005).
[31] R. Machleidt, F. Sammarruca, and Y. Song, Phys. Rev. C **53**, R1483 (1996).
[32] S. Frauendorf, Nucl. Phys. A **677**, 115 (2000).
[33] S. Frauendorf, Y. Gu, and J. Sun, Int. J. Mod. Phys. E **20**, 465 (2011).
[34] A. D. Ayangeakaa *et al.*, Phys. Rev. Lett. **110**, 102501 (2013).
[35] M. Doncel *et al.*, Phys. Rev. C **96**, 051304(R) (2017).
[36] O. Möller, N. Warr, J. Jolie, A. Dewald, A. Fitzler, A. Linnemann, K. O. Zell, P. E. Garrett, and S. W. Yates, Phys. Rev. C **71**, 064324 (2005).
[37] A. A. Pasternak *et al.*, Eur. Phys. J. A **13**, 435 (2002).
[38] M. Saxena *et al.*, Phys. Rev. C **90**, 024316 (2014).
[39] S. Frauendorf, Rev. Mod. Phys **73**, 463 (2001).
[40] S. Frauendorf, Phys. Rev. C **77**, 021304(R) (2008).
[41] X. Wang *et al.*, Phys. Lett. **102**, 122501 (2009).
[42] S. Zhu *et al.*, Phys. Rev. C **81**, 041306(R) (2010).
[43] L. M. Robledo, T. R. Rodríguez, and R. R. Rodriguez-Guzman, J. Phys. G: Nucl. Part. Phys. **46**, 013001 (2019).
[44] R. N. Bernard, L. M. Robledo, and T. R. Rodrìguez, Phys. Rev. C **93**, 061302(R) (2016).
[45] B. Bucher *et al.*, Phys. Rev. Lett. **118**, 152504 (2017).
[46] R. Licǎ *et al.*, Phys. Rev. C **97**, 024305 (2018).
[47] T. R. Rodríguez, A. Arzhanov, and G. Martinez-Pinedo, Phys. Rev. C **91**, 044315 (2015).